Nanoscale characterization of growth of secondary phases in off-stoichiometric CZTS thin films

Manoj Vishwakarma[1], Olesia M. Karakulina[2], Artem M. Abakumov[2], Joke Hadermann[2], B.R. Mehta[1*]

[1] Thin Film Laboratory, Department of Physics, IIT Delhi, New Delhi-110016, India
[2] EMAT, University of Antwerp, Groenenborgerlaan 171, B-2020 Belgium

Abstract:

The presence of secondary phases is one of the main issues that hinder the growth of pure kesterite Cu_2ZnSnS_4 (CZTS) based thin films with suitable electronic and junction properties for efficient solar cell devices. In this work, CZTS thin films with varied Zn and Sn content have been prepared by RF-power controlled co-sputtering deposition using Cu, ZnS and SnS targets and a subsequent sulphurization step. Detailed TEM investigations show that the film shows a layered structure with the majority of the top layer being the kesterite phase. Depending on the initial thin film composition, either about ~1μm Cu-rich and Zn-poor kesterite or stoichiometric CZTS is formed as top layer. X-ray diffraction, Raman spectroscopy and transmission electron microscopy reveal the presence of $Cu_{2-x}S$, ZnS and SnO_2 minor secondary phases in the form of nanoinclusions or nanoparticles or intermediate layers.

1. Introduction:

Cu_2ZnSnS_4 (CZTS) is a promising earth abundant, non toxic and low cost material having optical and electrical properties suitable for third generation photovoltaic applications [1]. It is a p-type semiconductor which has an optimal direct band gap of ~1.5 eV and a high absorption coefficient $\alpha \geq 10^4$ cm^{-1} that makes it suitable as an absorber layer in thin film solar cells [2-3]. CZTS has already been synthesized by various methods, including electron beam deposition [4], sputtering [5-6], thermal evaporation [7], spray pyrolysis [8], ink-based approaches [9], SILAR method [10], pulsed laser deposition [11], fast co-evaporation [12], sequential electro-deposition

process [13], sol-gel method [14-15], precipitation reaction in hot organic solutions [16] and chemical bath deposition [17] etc. Among these, the highest power conversion efficiency for pure CZTS based solar cell devices is reported to be 8.4% for a device obtained by thermal evaporation, while a Se doped CZTSSe based device obtained using a hydrazine pure-solution approach has achieved 12.6% [18-19]. Sputtering is a widely preferred method for large scale deposition due to its reproducibility. However, since different elements have different sputtering rates, using a CZTS alloy target normally results in a large deviation from the desired stoichiometry [20]. Controlling the stoichiometry is one of the most important goals to be achieved in a synthesis process and it plays a significant role in the final outcome in terms of efficiency of the solar cell [20]. As a multi-component material, CZTS has a quite complex phase diagram [21]. Those multiple components make it possible to tune the structural, optical and electrical properties by varying the composition, but this may result in the segregation of secondary phases [22]. Therefore, to further improve the efficiency of CZTS solar cells made through sputtering, it is important to systematically study the growth behaviour of secondary phases during CZTS growth [23]. In most of the reported studies the growth of the CZTS phase has been carried out close to Cu_2ZnSnS_4 stoichiometry [20]. In this paper, on the contrary, CZTS thin films have been intentionally grown in conditions resulting in compositions far away from those required for the stoichiometric CZTS phase, in order to study the growth of the secondary phases. We have synthesized CZTS thin films of varying composition by co-sputtering deposition followed by a sulphurization process. The presence of kesterite and the secondary phases was detected on a macroscopic scale by X-ray diffraction and Raman spectroscopy. The nanoscale characterization of their presence and distribution is carried out using advanced transmission electron microscopy on cross-sections of the films.

2. Experimental:

CZTS thin films were synthesized by radio frequency (13.56MHz) magnetron sputtering of Cu, ZnS and SnS precursor targets (2" inch diameter, 4mm thickness and 99.99% purity) on n-type Si (100) and glass substrates. The deposition rate (rf-power) of the targets was individually changed to vary the stoichiometry of CZTS thin films. The thin film samples S1, S2 and S3 were deposited with increasing rf-power of 40, 50 and 60W to SnS target, respectively and keeping other two targets of Cu and ZnS at constant power of 40W and 75W, respectively. Similarly, thin films S4, S5 and S6 were deposited with increasing rf-power of 80, 100, 110W to ZnS target, respectively and keeping rest of two targets Cu and SnS at constant rf-power of 40W and 50W, respectively. Prior to the deposition process, the substrate surface was cleaned by ultrasonication in acetone, propanol and deionised water followed by drying with nitrogen gas. The pre-deposition chamber was evacuated to $\sim 2.3 \times 10^{-6}$ mbar and the Ar-gas working pressure was maintained at$\sim$18-20 mTorr. During the growth of the CZTS thin films, the chamber was purged with Ar-gas flowing at 15 SCCM and the deposition time was 60 minutes for all samples. Thereafter, the films were placed in a two zone furnace for the sulphurization, where sulphur powder was placed in one zone at $\sim 240^{o}$C and the samples were placed in another zone at $\sim 560^{o}$C and annealed for 60 minutes. The flow of sulphur vapour was controlled by Ar carrier gas. The structural properties of the films were characterized by X-ray diffraction (Rigaku, ULTIMA IV, CuK$_{\alpha}$) and micro-Raman spectroscopy (Renishaw invia confocal Raman microscope, laser$\sim$532nm, power 1mW, 2400 lines per mm grating). The thin film lamellas for cross-sectional TEM analysis were prepared on Be supports using the focussed ion beam (FIB) technique. Prior to this, the surface of the thin films was examined by SEM. High resolution TEM (HRTEM), high angular annular dark field STEM (HAADF-STEM) images and energy dispersive X-ray spectroscopy combined with scanning TEM (EDX-STEM) were acquired at a FEI Osiris microscope operated at 200kV and equipped with a super-X detector.

3. Results:

3.1 Structural analysis

The two series of CZTS thin films with varied tin (S1-S3) and zinc (S4-S6) content were synthesized for the detailed study of the formation and distribution of the secondary phases. As a first step, the crystal structure and the presence of different phases were investigated using the macroscopic characterization techniques of X-ray diffraction and Raman spectroscopy. The Sn concentration is increased from sample S1 to sample S3 by increasing the rf-power on the SnS target. The XRD analysis of the S1-S3 thin film samples show that they primarily consist of the kesterite phase (Fig.1) as high intensity reflections are in agreement with the kesterite CZTS phase (PCPDFWIN No. 26-0575), whereas the less intense peaks can be attributed to $Cu_{2-x}S$ [24] (PCPDFWIN No. 850620) and SnO_2 [25](PCPDFWIN No. 721147). As the Sn concentration increases from S1 to S3, the presence of SnO_2 becomes more noticeable in the XRD spectra of S2 and S3. The Raman spectra of samples S1-S3 are shown in Fig 2. In all the samples peaks are observed at 338 cm^{-1} and 288 cm^{-1}, which correspond to the kesterite phase [26], while the peak detected at 473 cm^{-1} is attributed to $Cu_{2-x}S$ [27]. The CZTS thin films in the S4-S6 series were prepared with varied Zn content by increasing the rf-power of the ZnS precursor target. Fig.3 shows the XRD pattern of the CZTS thin film samples S4-S6, where all major peaks are in agreement with the kesterite CZTS phase. The only impurity of crystalline nature is SnO_2. Apart from CZTS, a very intense peak corresponding to $Cu_{2-x}S$ can be seen in the Raman spectra (Fig.4). The difference between the results obtained by XRD and Raman analysis is due to the inability of XRD to detect amorphous phases whereas Raman analysis is sensitive to both crystalline and amorphous phases.

3.2 EDX analysis of thin films S3 and S6

The overall chemical compositions of the S3 and S6 thin films were analysed by energy dispersive X-ray analysis (EDX). The stoichiometry parameters for the thin film sample S3 are: Cu/(Zn+Sn)~ 1.7, Zn/Sn~ 0.3 and S/(Cu+Zn+Sn)~ 0.6, while for the thin film sample S6 these values are ~ 1.4, 0.9 and 0.6, respectively. In terms of the overall chemical compositions in the film, sample S3 is Cu-rich and Sn-rich while sample S6 is Cu-rich.

3.3 TEM analysis of CZTS thin film sample S3

The Sn enriched S3 thin film is 2.6 μm thick and has a varied morphology (Fig.5a and 6a). Its cross-section image shows three main layers: a ~1 μm dense top layer (L1), a 0.5 μm intermediate layer (L2) and a 1 μm dense bottom layer (L3) (Fig.6a). Additionally, a 200 nm porous interface layer (L4) between the Si-substrate and CZTS thin film is observed. Fig.7(a) shows that the top layer (L1) consists of ~800 nm crystallites along with small 30-100 nm particles. The L2 layer contains 20-80 nm pores and is formed by 10-20 nm particles, while in the L3 layer there are 5-20 nm spherical and ~50×100 nm elongated particles (Fig.7b, c). This indicates a better crystallinity and large crystallite growth in the top layer L1 in comparison to the layers L2 and L3. The exposure of the top layer to the S vapour seems to assist in the crystallite growth. Most of the rings on the ring diffraction pattern of sample S3 can be either CZTS or sphalerite ZnS, except those with a d-value higher than 3.1 Å, i.e. (101) and (110), which cannot be ZnS and therefore confirm the presence of kesterite CZTS (Fig. 8a). STEM-EDX mapping was used to obtain the distribution of the elements within the cross-sectional lamella. The surface of the thin film is covered with 150-400 nm Cu_2S particles (Cu: S=66.3:33.7). The layer below (L1) consists of Cu, Zn, Sn, S elements having $\frac{S}{(Cu+Zn+Sn)} \approx 0.7$ ratio (Table.1). A similar composition is found in layer L3, which is separated from L1 by the Sn and O enriched layer L2. Since the tin and oxygen maps replicate each-other (Fig.9), it can be concluded that oxygen is present only in tin oxide form.

The presence of SnO_2 phase is also confirmed by electron diffraction and by the XRD pattern. Furthermore, layer L4 comprises mainly of SnO_2 phase, while in layer L3 SnO_2 is found in minor amount. In order to figure out the origin of the 30-100 nm particles in the L1 layer (as visible in Fig.7a), this region was thoroughly studied at a higher magnification. The area free of the particles has Cu: Zn: Sn: S = 2.64:0.67:1.20:3.49 stoichiometry with $\frac{Cu}{(Zn+Sn)} = 1.4$, $\frac{Zn}{Sn} = 0.6$ and $\frac{S}{(Cu+Zn+Sn)} = 0.8$ ratios, which shows the presence of the Cu-rich and Zn-poor kesterite phase in layer L1 (Fig.10). The areas covered with bright particles in the HAADF-STEM image have more Cu and less S (Cu: Zn: Sn: S = 3.15:0.55:1.04:3.26) than the area free of particles. It means that this region contains $Cu_{2-x}S$ particles along with CZTS phase.

3.4 TEM analysis of CZTS thin film sample S6

The S6 thin film is 2.2 μm thick and by analogy with sample S3, three layers can be distinguished, i.e. a 0.8 μm top layer (L1), 1.2 μm intermediate layer (L2) and 0.2 μm bottom interface layer (L3) (Fig.6b). The L1 layer comprises of loosely packed 200-400 nm crystallites with 200-300 nm pores in between (Fig.11a). Layers L2 and L3 are formed by ~10-50 nm crystallites and contain 15-30 nm and 100-200 × 30 nm elongated pores, respectively (Fig.11b, c). By means of SAED it was revealed that the crystallites residing in L1 correspond to the kesterite phase with approximate unit cell parameters a=5.3 Å and c=11.0 Å (Fig.8b). The L2 layer also contains the CZTS phase along with SnO_2 (Fig.8d). In comparison to L2, it is hardly possible to distinguish the tin oxide reflections in the electron diffraction ring pattern of the L1 layer. Therefore, it can be concluded that kesterite is the main phase in L1 (Fig.8c). On the EDX-STEM maps the elemental distribution in layer L1 is more uniform than in the other layers (Fig.12). However, Zn segregates at the top of the CZTS crystallites, forming 100-200 nm ZnS particles. The Cu content in layer L2 is higher than in L1 (Table.2), since it contains $Cu_{2-x}S$, which can be clearly distinguished in the

HAADF-STEM image as bright ~200 nm particles (Fig.12 a, b). The presence of $Cu_{2-x}S$ is consistent with the Raman spectrum (Fig.4). The O content is insignificant and mainly resides at the bottom of the thin film (L3) in tin oxide form (Fig.12c). The EDX-STEM maps of the L1 layer show that the distribution of the elements is uniform in the regions of the CZTS crystallites (Fig.13). The element content in this region is Cu: Zn: Sn: S = 2.21: 1.21: 1.07: 3.51 and the ratios are $\frac{Cu}{(Zn+Sn)} = 0.97$, $\frac{Zn}{Sn} = 1.13$ and $\frac{S}{(Cu+Zn+Sn)} = 0.78$, which is close to Cu_2ZnSnS_4 composition.

4. Discussion

As stated earlier, the deposition of CZTS thin films in this study was deliberately done under conditions far away from those required for stoichiometric compositions. The complex nature of the kesterite phase formation was demonstrated by phase analysis as a function of the initial compositions. XRD spectra substantiated that the SnO_2 phase increases with increasing Sn content, i.e. from sample S1 to S3, but it was insignificant in the samples with increasing Zn content (S4 to S6). A Cu-rich composition ($\frac{Cu}{(Zn+Sn)} > 1$) results in a porous sulphurized film [28], as is also found in our TEM analysis of sample S3 (layer L2) and sample S6 (layer L3). This is because of the fact that Cu is known to react easily with sulphur vapour [28-29]. Here, we see the effect of the $\frac{Cu}{(Zn+Sn)}$ ratio: $\frac{Cu}{(Zn+Sn)} \sim 1.7$ results in a higher percentage of kesterite phase layer (~1μm thickness) (sample S3) than $\frac{Cu}{(Zn+Sn)} \sim 1.4$ which results in an only ~800 nm thick kesterite CZTS layer (sample S6) [28]. A higher Cu-concentration resulted into a larger crystallite size of ~800 nm in sample S3 and ~200 nm in sample S6 but Cu-rich composition also gives a higher percentage of $Cu_{2-x}S$. The formation of CZTS is initiated with the formation of Cu_2SnS_3 from the reaction of $Cu_{2-x}S$ with SnS_2, then the subsequent reaction with ZnS results in the formation of $Cu_2 ZnSnS_4$ [29-30-31]. Since SnS is highly volatile in nature at a temperature over ~400°C, the loss of SnS becomes inevitable and results in

phase separation, $Cu_2ZnSnS_4(s) \leftrightarrow Cu_2S(s) + ZnS(s) + SnS(g) + \frac{1}{1}S_2(g)$[32]. The CZTS

samples were annealed at ~560°C for 60 minutes, which can be a possible cause of the

appearance of $Cu_{2-x}S$ amorphous phase particles in sample S3 (Fig.9) and ZnS particles along

with $Cu_{2-x}S$ particles in sample S6 on the top surface (Fig.12). According to the TEM results

(Fig.10), the surface and L1 layer of sample S3 contain regions with $Cu_{2-x}S$ and SnO_2

composition. The $Cu_{2-x}S$ particles residing on the top surface of the thin film (S3) are non-

uniformly distributed. SnO_2 particles are observed in the intermediate layer and near the

bottom interface (Fig.9, 10). The results of the present study indicate that the Zn/Sn ratio is

an important parameter determining the stoichiometric and uniformity of the kesterite phase

in the top layer. Beside the bulk phase and grains size of the absorber layer, the stoichiometry

of the top layer is another crucial factor in deciding photovoltaic device performance [33]. The

top layer (L1) of S3 is Cu rich and Zn poor, while for sample S6 it is Cu-rich and Zn-rich, so

the resultant compositions of the top layer are different from the rest of the film. Due to the

high absorption coefficient of the CZTS absorber layer, more than 90% of the incident

photons are absorbed in the first ~ 200nm (from the top junction side) of the CZTS layer [33].

Therefore, the phase purity of the top layer determines the overall photovoltaic device

performance. However, the overall initial composition of the thin film determines the

formation of kesterite phase along with possible secondary phases. The initial composition

also affects the thickness of the top layer. This work confirms that the stoichiometry of the as

deposited CZTS thin film and the sulphurization conditions are vital for obtaining a single

phase CZTS absorber layer.

5. Conclusion

The present study shows that, after the sulphurization step, CZTS films with a starting

composition far away from the stochiometric value comprise of different layers with different

morphology, composition and secondary phases. The top layer of the CZTS thin films always

contains kesterite phase. $Cu_{2-x}S$, ZnS and SnO_2 nanoscale crystallites are present in the intermediate layer and at the interface between CZTS and the substrate. The thickness of the top kesterite layer and the crystallite size is observed to be related to Zn/Sn concentration in the as deposited thin film. Control over the initial Zn/Sn ratio is important for achieving uniformity and purity of the kesterite phase, especially in the top layer.

Acknowledgements

References

1. K. Woo, Y. Kim and J. Moon, Energy and Environmental Science, 5, 5340 (2012).
2. J. P. Leitao, N. M. Santos, P. A. Fernandes, P. M. P. Salome, A. F. da Cunha, J. C. Gonzalez, G. M. Ribeiro, and F. M. Matinaga, Physical Review B, 84, 024120 (2011).
3. J. J. Scragg, P. J. Dale and L. M. Peter, Electrochemistry Communications, 10, 639 (2008).
4. H. Araki, A. Mikaduki, Y. Kubo, T. Sato, K. Jimbo, W. S. Maw, H. Katagiri, M. Yamazaki, K. Oishi and A. Takeuchi, Thin solid films, 517, 1457 (2008).
5. M. Xie, D. Zhuang, M. Zhao, Z. Zhuang, L. Ouyang, X. Li and J. Song, International Journal of Photoenergy, 2013, 1 (2013).
6. J. S. Seol, S. Y. Lee, J. C. Lee, H. D. Nam and K. H. Kim, Solar Energy Material & Solar Cell, 75, 155 (2003).
7. K. Wang, O. Gunawan, T. Todorov, B. Shin, S.J. Chey, N. A. Bojarczuk, D. Mitzi and S. Guha, Applied Physics Letters, 97, 143508 (2010).
8. M. Patel, I. Mukhopadhyay and A. Roy, Journal of Physics D: Applied Physics, 45, 445103 (2012).
9. X. Sheng, L. Wang, Y. Tian, Y. Luo, L. Chang and D. Yang, Journal of Materials Science: Materials in Electronics, 24, 548 (2013).
10. S. S. Mali, P. S. Shinde, C. A. Betty, P. N. Bhosale, Y. W. Oh and P. S. Patil, Journal of Physics and Chemistry of Solids, 73, 735 (2012).
11. A. V. Moholkar, S. S. Shinde, A. R. Babar, K. U. Sim, Y. Kwon, K. Y. Rajpure, P. S. Patil, C. H. Bhosale and J. H. Kim, Solar Energy, 85, 1354 (2011).
12. B. A. Schubert, B. Marsen, S. Cinque, T. Unold, R. Klenk, S. Schorr and H. W. Schock, Progress in Photovoltaics: Research and Applications, 19, 93 (2011).
13. C. Y. Su, C. Y. Chiu and J. M. Ting, Scientific Reports, 5, 9291 (2015).
14. B. L. Guo, Y. H. Chen, X. J. Liu, W. C. Liu, and A. D. Li, AIP Advances, 4, 097115 (2014).
15. X. Yu, A. Ren, F. Wang, C. Wang, J. Zhang, W. Wang, L. Wu, W. Li, G. Zeng and L. Feng, International Journal of Photoenergy, 2014, 1 (2014).
16. S. C. Riha, B. A. Parkinson and A. L. Prieto, Journal of American Chemical Society, 131, 12054 (2009).
17. E. P. Subramanian, G. Rajesh, N. Muthukumarsamy, M. Thambidurai, V. Ashokan and D. Velauthapillai, Indian Journal of Pure and Applied Physics, 52, 620 (2014).
18. B. Shin, O. Gunawan, Y. Zhu, N. A. Bojarczuk, S. J. Chey and S. Guha, Progress in Photovoltaics: Research and Applications, 21, 72 (2013).
19. W. Wang, M. T. Winkler, O. Gunawan, T. Gokmen, T. K. Todorov, Y. Zhu, and D. B. Mitzi, Advanced Energy Materials, 4, 1301465 (2014).
20. N. Muhunthan, O. P. Singh, S. Singh, and V. N. Singh, International Journal of Photoenergy, 2013, 1 (2013).
21. H. Du, F. Yan, M. Young, B. To, C. S. Jiang, P. Dippo, D. Kuciauskas, Z. H. Chi, E. A. Lund, C. Hancock, W. M. Hlaing OO, M. A. Scarpulla and G. Teeter, Journal of Applied Physics, 115, 173502 (2014).
22. M. Bar, B. A. Schubert, B. Marsen, S. Schorr, R. G. Wilks, L. Weinhardt, S. Pookpanratana, M. Blum, S. Krause, Y. Zhang, W. Yang, T. Unold, C. Heske, and H. W. Schock, Physical Review B, 84, 035308 (2011).
23. W. Bao and M. Ichimura, International Journal of Photoenergy 2015, 1 (2015).
24. M. Saranya, C. Santhosh, R. Ramachandran, and A. N. Grace, Journal of Nanotechnology, 2014, 1 (2014).
25. G. E. Patil, D. D Kajale, V. B. Gaikwad and G. H. Jain, International Nano Letters, 2, 1 (2012).
26. C. Y. Su, C. Y. Chiu & J. M. Ting, Scientific Reports, 5, 9291 (2015).

27. T. T. Thu Nguyen, H. Y. Shin, G. Y. Kim, J. R. Kim, W. Jo and S. Yoon, Journal of the Korean Physical Society, 66, 117 (2015).
28. C. H. Tsai, J. M. Ting and R. R. Wang, Acta Materialia, 59, 349 (2011).
29. R. Schurr, A. Holzing, S. Jost, R. Hock, T. Vo, J. Schulze, A. Kirbs, A. Ennaoui, M. L. Steiner, A. Weber, I. Kotschau, H. W. Schock, Thin Solid Films, 517, 2465 (2009).
30. A. Alvarez, S. Exarhos, L. Mangolini, Materials Letters, 165, 41 (2016).
31. J. J. Scragg, T. Ericson, T. Kubart, M. Edoff and C. P. Bjorkman, Chemistry of Materials, 23, 4625 (2011).
32. A. R. Jeong, W. Jo, S. Jung, J. Gwak, and J. H. Yun, Applied Physics Letters, 99, 082103 (2011).
33. J. Zhong, Z. Xia, M. Luo, J. Zhao, J. Chen, L. Wang, X. Liu, D. J. Xue, Y. B. Cheng, H. Song and J. Tang, Scientific Reports, 4, 6288 (2014).

Manuscript Tables and Figures

Table.1 Cu/Zn/Sn/S content in layers L1, L2, L3 and L4 of S3 sample (in at. %).

Element	Layer L1	Layer L2	Layer L3	Layer L4
Cu	36.8	34.6	39.3	45.5
Zn	7.4	4.6	6.6	3.0
Sn	14.2	30.0	16.2	22.3
S	41.6	30.8	37.9	29.2

Table.2 Cu/Zn/Sn/S content in layers L1, L2 and L3 of S6 sample (in at. %).

Element	Top layer L1	Dense layer L2	Bottom Layer L3
Cu	31.96	34.83	23.28
Zn	15.03	11.72	15.27
Sn	10.95	16.87	26.16
S	42.06	36.58	35.29
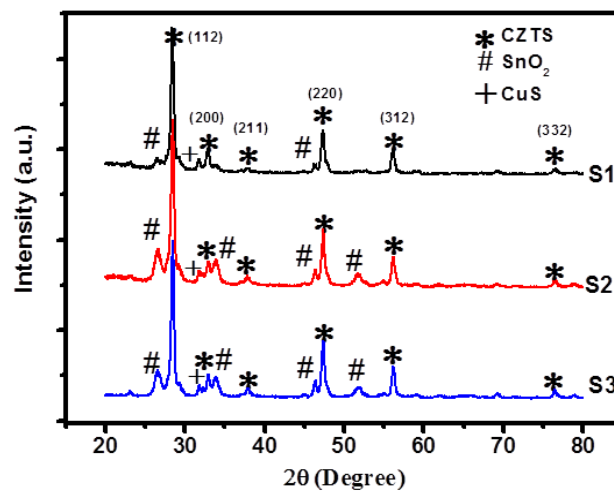
Fig.1 X-ray diffraction patterns of CZTS thin films with varied Sn concentration (S1-S3).
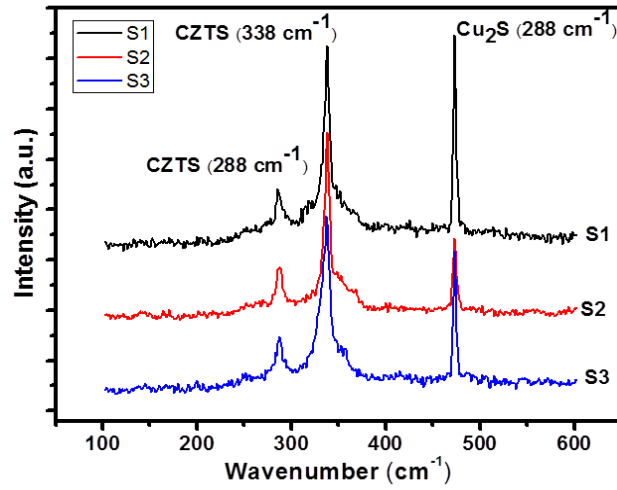
Fig.2 Raman spectra of CZTS thin films with varied Sn concentration (S1-S3).
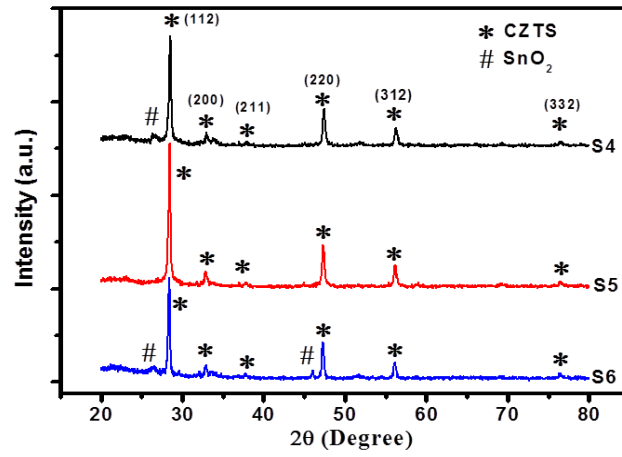
Fig.3 X-ray diffraction patterns of CZTS thin films with varied Zn concentration (S4-S6).
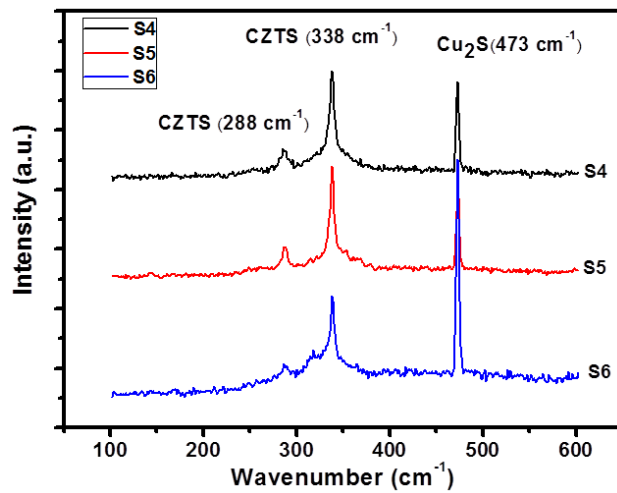
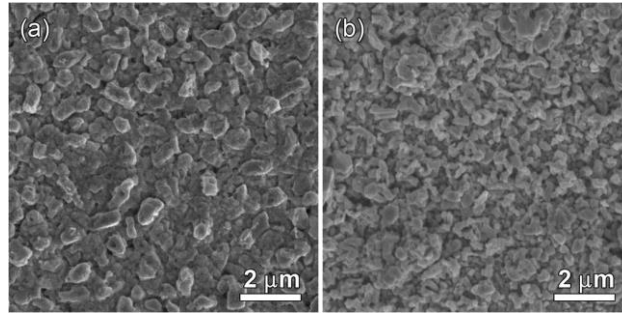Fig.4 Raman spectra of CZTS thin films with varied Zn concentration (S4-S6).

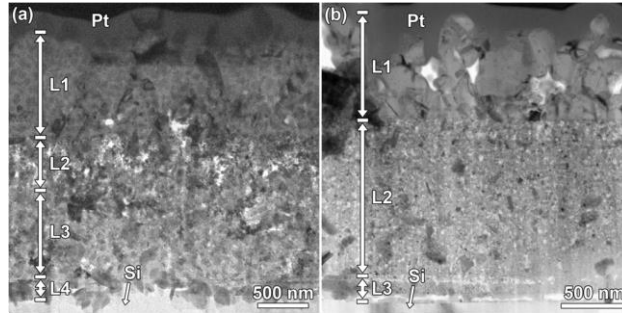Fig.5 SEM images of the surface of (a) S3 and (b) S6 samples.

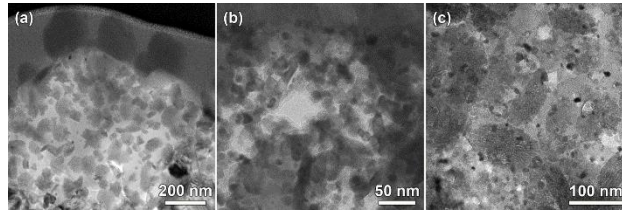Fig.6. TEM image of the cross-section lamella of (a) S3 and (b) S6 thin films.

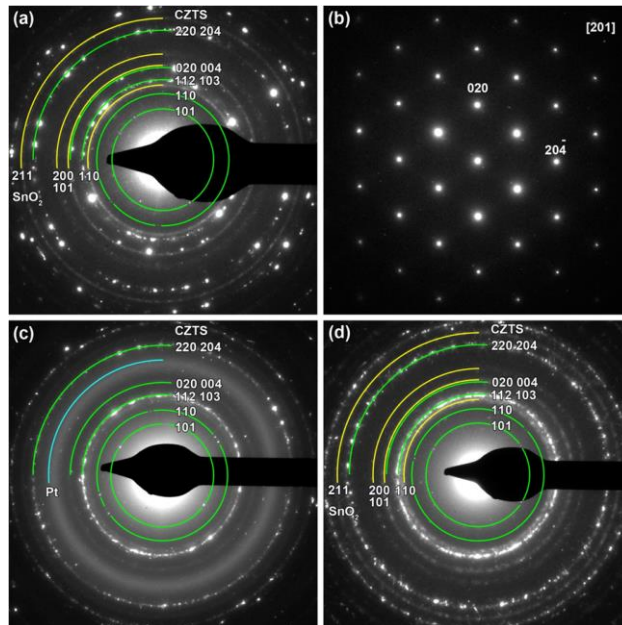Fig.7 (a) TEM images of L1 (top layer), (b) L2 and (c) L3 layers of S3 sample.

Fig.8 The selected area ring diffraction patterns of (a) the sample S3, (c) layer L1 and (d) layer L2 of S6. Green and yellow curves correspond to kesterite CZTS and SnO_2, respectively. (b) In zone SAED of crystallite from L1 layer of sample S6, corresponding to the [201] diffraction pattern of kesterite.
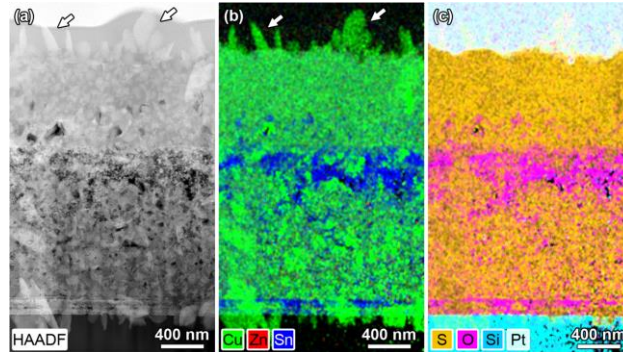

Fig.9 (a) HAADF-STEM image and (b, c) EDX-STEM maps of sample S3. The maps are presented in atomic fractions. Cu_2S particles reside at the top (marked by arrows).
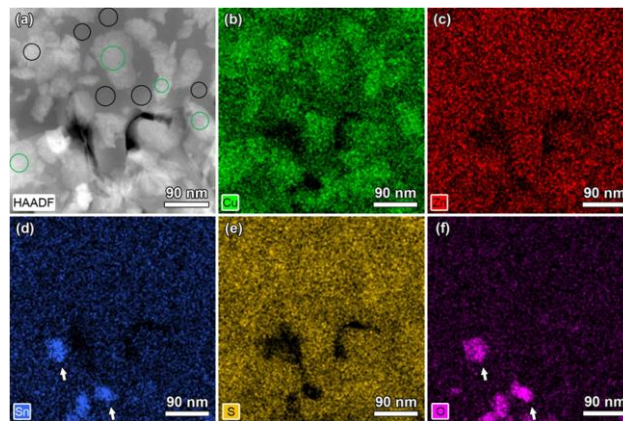

Fig.10 (a) HAADF-STEM image and (b-f) EDX-STEM Cu/Zn/Sn/S/O element maps of layer L1 in sample S3.The maps are presented in counts. The areas used for the element content estimation of kesterite phase (black circles) and Cu-enriched areas (green circles) are marked in (a). The SnO_2 particles are seen in Sn and O maps (white arrows).
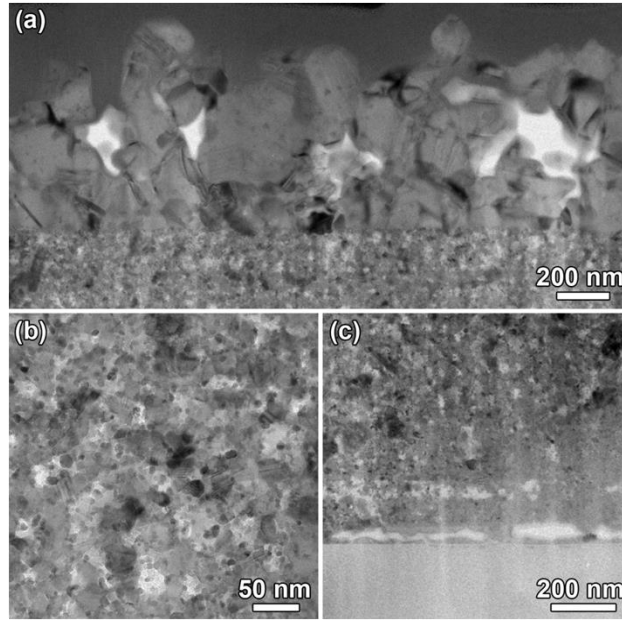
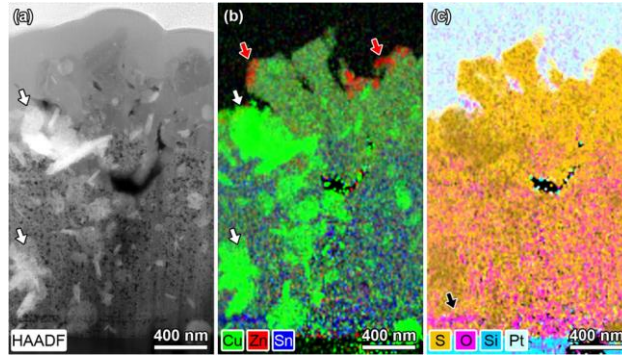Fig.11 TEM images of (a) top (L1), (b) middle (L2) and (c) bottom (L3) layers of S6 sample.

Fig.12 (a) HAADF-STEM image and (b, c) EDX-STEM maps of sample S6. The maps are presented in atomic fractions. ZnS particles reside at the top (marked by red arrows). The $Cu_{2-x}S$ particles can be distinguished in HAADF image and Cu map (white arrows). Oxygen is mainly situated at the bottom (black arrows in (c)).
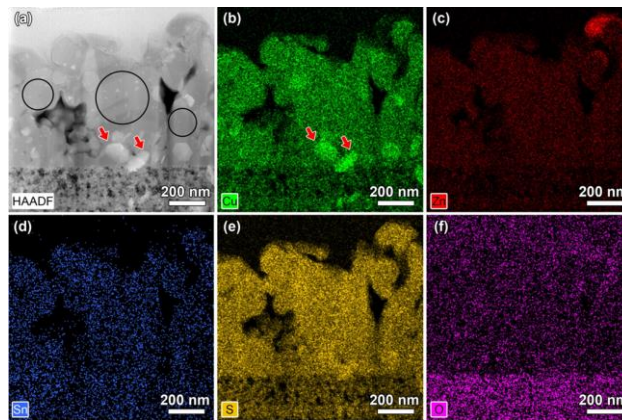

Fig.13 (a) HAADF-STEM image and (b-f) EDX-STEM Cu/Zn/Sn/S/O element maps of layer L1 in sample S6. The maps are presented in counts. The areas used for the element content estimation of kesterite phase (black circles) are marked in (a). The $Cu_{2-x}S$ particles can be distinguished in HAADF image and Cu map (marked by red arrows).

Nanoscale characterization of growth of secondary phases in off-stoichiometric CZTS thin films

Manoj Vishwakarma[1], Olesia M. Karakulina[2], Artem M. Abakumov[2], Joke Hadermann[2], B.R. Mehta[1*]

Graphical Abstract

The detailed TEM investigations of the off-stoichiometric CZTS thin films shows a multilayer structure with kesterite phase in top layer (T) and secondary phases (SnO_2, Cu_2S etc) in intermediate (I), bottom (B) and substrate interfacial (S) layers (the multilayer structure for sample S3 is shown here). The crystallite size and the stoichiometry of the top layer can be controlled by changing the initial composition of the as deposited layer.